Volume 14 | Number 9 | 7 March 2018 | Pages 1501–1738

# Soft Matter

rsc.li/soft-matter-journal

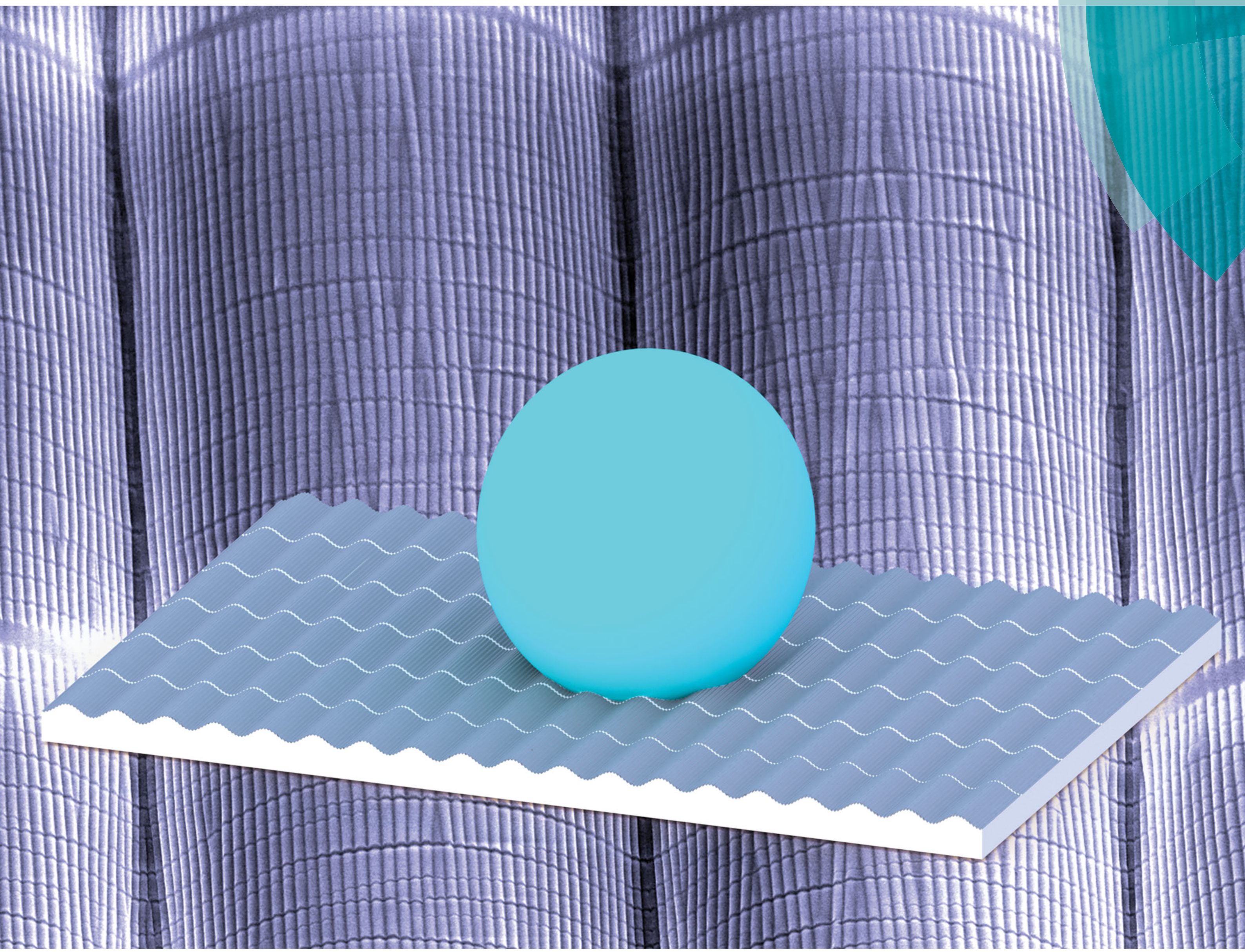

ISSN 1744-6848

ROYAL SOCIETY OF **CHEMISTRY**

PAPER
Jie Yin *et al.*
Small degree of anisotropic wetting on self-similar hierarchical wrinkled surfaces

Soft Matter

PAPER

View Article Online
View Journal | View Issue

Check for updates

Cite this: *Soft Matter*, 2018, **14**, 1517

# Small degree of anisotropic wetting on self-similar hierarchical wrinkled surfaces†

Gaojian Lin,[a] Qiuting Zhang,[a] Cunjing Lv,[b] Yichao Tang[a] and Jie Yin *[a]

We studied the wetting behavior of multiscale self-similar hierarchical wrinkled surfaces. The hierarchical surface was fabricated on poly(dimethylsiloxane) (PDMS) substrates by manipulating the sequential strain release and combined plasma/ultraviolet ozone (UVO) treatment. The generated structured surface shows an independently controlled dual-scale roughness with level-1 small-wavelength wrinkles (wavelength of 700–1500 nm and amplitude of 50–500 nm) resting on level-2 large-wavelength wrinkles (wavelength of 15–35 μm and amplitude of 3.5–5 μm), as well as accompanying orthogonal cracks. By tuning the aspect ratio of hierarchical wrinkles, the degree of wetting anisotropy in hierarchical wrinkled surfaces, defined as the contact angle difference between the parallel and perpendicular directions to the wrinkle grooves, is found to change between 3° and 9°. Through both experimental characterization (confocal fluorescence imaging) and theoretical analyses, we showed that the wetting state in the hierarchical wrinkled surface is in the Wenzel wetting state. We found that the measured apparent contact angle is larger than the theoretically predicted Wenzel contact angle, which is found to be attributed to the three-phase contact line pinning effect of both wrinkles and cracks that generates energetic barriers during the contact line motion. This is evidenced by the observed sudden drop of over 20° in the static contact angles along both perpendicular and parallel directions after slight vibration perturbation. Finally, we concluded that the observed small degree of wetting anisotropy in the hierarchical wrinkled surfaces mainly arises from the competition between orthogonal wrinkles and cracks in the contact line pinning.

Received 9th November 2017,
Accepted 10th January 2018

DOI: 10.1039/c7sm02208e

rsc.li/soft-matter-journal

## 1. Introduction

Hierarchical structured surfaces with multiscale roughness from the nanoscale to the macroscale are often found in nature to provide extraordinary properties, such as non-wettability and self-cleaning in lotus leaves,[1] strong adhesion in gecko's feet,[2] and structural color in butterfly wings.[3] Fascinated by these intriguing properties, researchers have devoted great efforts to reproduce the functionalities by mimicking these biological hierarchical structured surfaces through a variety of fabrication methods, including replica molding,[4] etching,[5] lithography,[6] chemical deposition,[7] and colloidal assembly.[8]

Due to its ease in materials handling, fabrication, and control,[9,10] surface wrinkling has attracted growing research interest in the past two decades and has been proven to be a facile approach to generate various controllable surface topographies with dynamic tunability and multifunctionality,[11–16] including but not limited to adaptive hierarchical surfaces[17,18] with dynamically tunable properties in wetting and optics.[9,10,19] Among them, Efimenko *et al.*[17] first demonstrated the formation of nested, hierarchical wrinkled surfaces on oxidized poly(dimethylsiloxane) (PDMS) elastomers under high compressive strain. By coating gold film on extremely pre-strained elastomer, Cao *et al.*[19] generated high-aspect-ratio hierarchical ridged surfaces with both tunable wetting and optical properties controlled by simple strain. Structured hierarchical wrinkled surfaces have also been achieved by integrating micro/nano-structures (*e.g.* pillars or particles) onto single-period micro-wrinkled elastomers,[9,10,20,21] which exhibited similar switchable wetting and/or optical behavior. Very recently, based on the sequential wrinkling strategy,[22] we have successfully fabricated multiscale self-similar hierarchical wrinkled surfaces on plasma treated PDMS elastomer with their surface features crossing from nanoscale (wrinkles with wavelength of 400–950 nm) to microscale (wrinkles with wavelength of 3–5 μm).[23] Such multiscale self-similar hierarchical wrinkles have demonstrated unique performances in tunable optical properties and controllable droplet motion.[23]

Meanwhile, anisotropic wetting is a fascinating feature on natural and engineered anisotropic patterned surfaces, which has attracted researchers' interest for decades due to its potential application in directional water transport and water collection.[24] Intriguing examples in nature include directional flow in a rice

[a] *Applied Mechanics of Materials Laboratory, Department of Mechanical Engineering, Temple University, 1947 North 12th Street, Philadelphia, PA 19122, USA. E-mail: jieyin@temple.edu*

[b] *Department of Engineering Mechanics, Tsinghua University, Beijing, 100084, China*

† Electronic supplementary information (ESI) available. See DOI: 10.1039/c7sm02208e

leaf[25] and Namib dessert grass,[26] as well as radial water shedding in butterfly wing from its body center.[27] The anisotropic wettability can be achieved by either heterogeneous chemical patterning or anisotropic surface morphology or combined both. Chemically, through line-patterned hydrophobic/hydrophilic area, researchers have demonstrated the tunability in anisotropic wetting by adjusting the line width and interval.[28–31] Physically, anisotropic wetting can be realized by engineering surfaces with anisotropic topographical features. Theoretical studies of anisotropic wetting properties on various shapes of single-period parallel grooved microstructures showed that the wetting anisotropy strongly depends on the specific topographical features and wetting state.[32]

As one of the highly topographical anisotropic structures, studies have demonstrated the dynamically tunable anisotropic wetting of wrinkles through simply stretching the wrinkled surfaces. Chung *et al.*[33] first studied the tunable anisotropic wetting on single-period micro-wrinkled surfaces through simple mechanical strains. They showed a transition from isotropic (flat) to anisotropic wetting (micro-wrinkled) through strain-controlled wrinkling, where the difference of the contact angles between two orthogonal directions could reach 50°. Lee *et al.*[25] studied the anisotropic wetting on wavy surfaces covered with nanoparticles, similar to the hierarchical structure of the rice leaf surface. They showed that by increasing the roughness of nanoparticle layer on the wrinkled elastomer, the dynamic wetting behavior can transit from anisotropic/pinned to anisotropic/rollable, and to isotropic/rollable state.

Despite the advancement, the experimental study and theoretical understanding of anisotropic wetting behavior and wetting state on hierarchical wrinkled surfaces still remain largely unexplored.[33,34] Compared to single-period micro-wrinkles, how the structural hierarchy in multiscale wrinkled surfaces influences their wetting state and anisotropic wetting behavior alongside its underlying wetting mechanism is largely unknown. Several theoretical studies on the wetting property of multiscale hierarchical wrinkled surfaces predict the possibility of forming superhydrophobic surfaces by optimizing the dimension of wrinkles at each hierarchical level,[35,36] however, it remains to be examined experimentally.

In this paper, we focus on the self-similar hierarchical wrinkled surfaces. Compared to most previously studied wrinkling-based hierarchical structured surfaces without self-similarity, including pillars[9,10] or particles[25] on single-period wrinkles, and pre-imprinted line patterns on herringbone-like wrinkles,[37] the self-similar hierarchical wrinkled surface presents the most anisotropic morphological characteristics.[31] Furthermore, the self-similarity could provide a better control of the hierarchical features in each level, as well as an idealized model system for examining related developed theoretical models. Here, we extended our recent study of sequential wrinkling[23] to generate self-similar hierarchical wrinkles with one order higher multi-scale hierarchy crossing from hundreds of nanometers to tens of microns, and explored their potential anisotropic wetting behavior through both experimental and theoretical analysis. We first discussed the tunable geometrical dimension in multi-scale hierarchical wrinkles by manipulating the treatment time, as well as investigated its effect in the wetting anisotropy of hierarchical wrinkled surfaces. We examined the possible wetting state of the tunable multiscale hierarchical wrinkled surface through both surface free-energy based theoretical models and experimental confocal imaging visualization. Then we analyzed the observed anisotropic wetting behavior through the developed theoretical model by calculating the free energy change during the three-phase contact line moving, as well as experimental examination. Last, we concluded with some remarks on the competition between wrinkles and orthogonal cracks in line pinning in determining its anisotropic wetting behavior of a hierarchical wrinkled surface.

## 2. Experimental section

### Generation of hierarchical wrinkled surfaces *via* sequential wrinkling

Following the procedures in ref. 23, a hierarchical wrinkled surface with a larger multi-scalability crossing two hierarchical levels is fabricated by sequential plasma and UVO treatment of the PDMS substrate. Fig. 1 shows the schematics on the

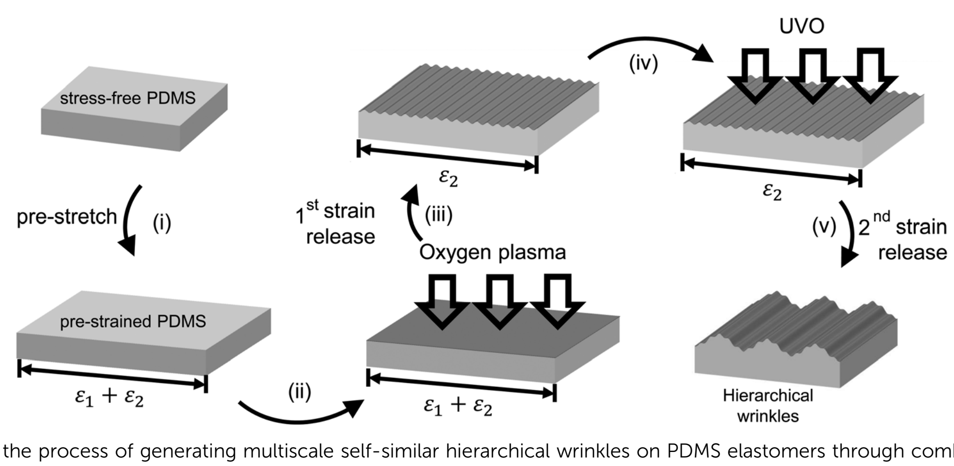


Fig. 1 Schematics of the process of generating multiscale self-similar hierarchical wrinkles on PDMS elastomers through combined plasma and UVO treatment and two-step strain release.

fabrication process of PDMS samples with hierarchical surface wrinkles by following two sequential steps. In the 1st step, a thin sheet of PDMS substrate with thickness of $\approx$2 mm is initially pre-stretched uni-axially to a strain of $\varepsilon_{pre} = \varepsilon_1 + \varepsilon_2$ using a home-made stretching device, followed by oxygen plasma treatment (Harrick, model PDC-32G) at a power of 18 watts for time $T_1$ (about 4–10 minutes). This creates a thin stiff layer of amorphous silica on the surface of the PDMS substrate. Then the plasma treated PDMS substrate is partially released for the first time with a strain of $\varepsilon_1$ to generate level-1 sub-micron wrinkles $\lambda_1$ (typically several hundred nanometers). In the 2nd step, the wrinkled PDMS is further treated with UVO (Jelight, model 18) for a second time with time $T_2$ (about 30–60 minutes) to create a much thicker silica layer than that generated in the 1st step, followed by the complete release of the pre-stretched strain, *i.e.* a released strain of $\varepsilon_2$. This leads to the formation of hierarchical wrinkles with a much higher multi-scalability crossing each level, where level-1 sub-micron wrinkles generated in the 1st step are superposed on the level-2 micro-wrinkles ($\lambda_2$) generated in the 2nd step ($\lambda_2$ is on the order of tens of microns, rather than few microns through plasma treatment reported in ref. 23).

#### Surface topography characterization

Scanning electron microscopy (SEM) images were taken by FEI Quanta 450FEG in low vacuum mode at an acceleration voltage of 10 kV. Tapping mode atomic force microscopy (AFM) imaging was applied to quantify the surface 3D topography of the level-1 sub-micron wrinkled structure in ambient conditions using a Dimension Icon (BrukerNano, Santa Barbara, CA) and a nano-sized silicon tip (nominal end radius $R \sim 10$ nm, spring constant $k \sim 42$ N m$^{-1}$, NCHV-A, BrukerNano). For each sample, a minimum of five different locations were imaged to confirm the repeatability. The level-2 micro-wrinkles were imaged using non-contact white light interferometry (Zygo NewView 7300 Optical Profilometer). A Zeiss Axio Imager M2m optical microscope was used with 20× objective for optical imaging.

#### Confocal imaging

Wrinkled PDMS samples with 5 μL water droplets containing fluorescently labelled microparticles (Micro particles based on melamine resin, FITC marked, 1 μm in diameter, Sigma-Aldrich) on top were observed using confocal laser scanning microscopy (LSM 510, Zeiss, Germany; 40× objective, N.A. = 0.55) to record the *z*-stacks of the samples. The fluorescence was excited by a 488 nm laser. Two signals were recorded from each scan. The conventional reflectivity signal showed the surface topology and the fluorescence signal showed the existence of water. The fluorescence signal was superimposed on the reflectivity signal for a better view.

#### Contact angle (CA) measurements

The contact angles were taken with ramé-hart Model 260 Standard Contact Angle Goniometer at ambient temperature. For the measurement of the static contact angle, a 5 μL deionized (DI) water droplet was first deposited gently on the hierarchical wrinkled surface using an automatic pipet, and then a photograph of the water droplet rested on the sample surface was taken immediately using the goniometer camera. The advancing and receding contact angles were measured by smoothly increasing or decreasing the volume of the droplet volume. The CA was measured from the photograph by the software. For each sample, at least three points were measured in two directions: perpendicular to and parallel with the wrinkled groove direction and an average value was recorded. To examine the stability of the measured contact angles after perturbation, the sample with a water droplet on top was clamped with a tweezer and manually shaken up and down at a frequency of $\sim$3 Hz and amplitude of 1–2 cm for 3 seconds. Then the sample was placed back on goniometer and CAs of two directions were measured. This procedure was repeated until the measured contact angles of both directions became unchanged. The experiments were conducted at three different locations of each sample to validate the consistency.

## 3. Results and discussion

### 3.1 Tunable dimensions of multiscale hierarchical wrinkles

Fig. 2a shows the representative SEM images of a hierarchical wrinkled surface after sequential strain release and plasma-UVO treatment with $\varepsilon_1 = \varepsilon_2 = 25\%$, $T_1 = 5$ min, and $T_2 = 40$ min in a high (left) and low (right) magnified resolution, respectively. The corresponding cross-section profiles are shown in Fig. 2b and c. It shows that the sub-micron wrinkles at level 1 have an average amplitude $A_1$ and wavelength $\lambda_1$ of $A_1 \approx 297$ nm and $\lambda_1 \approx 800$ nm (measured by AFM); while the micro-wrinkles at level 2 have an average amplitude and wavelength of $A_2 \approx 4.5$ μm and $\lambda_2 \approx 25.8$ μm (measured by the white light interferometry).

It is well known that the geometrical size of the single-period wrinkles (wrinkling wavelength $\lambda$ and amplitude $A$) for a thin film rested on a soft substrate can be well predicted by the following theoretical model,[38] *i.e.*

$$\lambda = 2\pi t_f \left(\frac{\bar{E}_f}{3\bar{E}_{sub}}\right)^{\frac{1}{3}} \quad (1)$$

$$A = \frac{\lambda}{\pi}\sqrt{(\varepsilon - \varepsilon_{cr})} \quad (2)$$

where $t_f$ is the film thickness of the oxidation layer after plasma or UVO treatment, $\bar{E} = E/(1-\nu^2)$ is the plane-strain modulus with $E$ being the Young's modulus and $\nu$ being the Poisson's ratio, respectively. The subscripts '*f*' and 'sub' refer to the stiff film and soft substrate, respectively. $\varepsilon$ is the released strain and $\varepsilon_{cr}$ is the critical wrinkling strain given by[38]

$$\varepsilon_{cr} = -\frac{1}{4}\left(\frac{3\bar{E}_{sub}}{\bar{E}_f}\right)^{\frac{2}{3}} \quad (3)$$

The dimension of each level in the hierarchical wrinkles can be controlled independently by manipulating the treatment time and released strain in terms of eqn (1) and (2). Fig. 3a and b show that the dimension of each hierarchical wrinkle can be tuned in the range of $\lambda_1 \approx 700$–1500 nm and $A_1 \approx 50$–500 nm

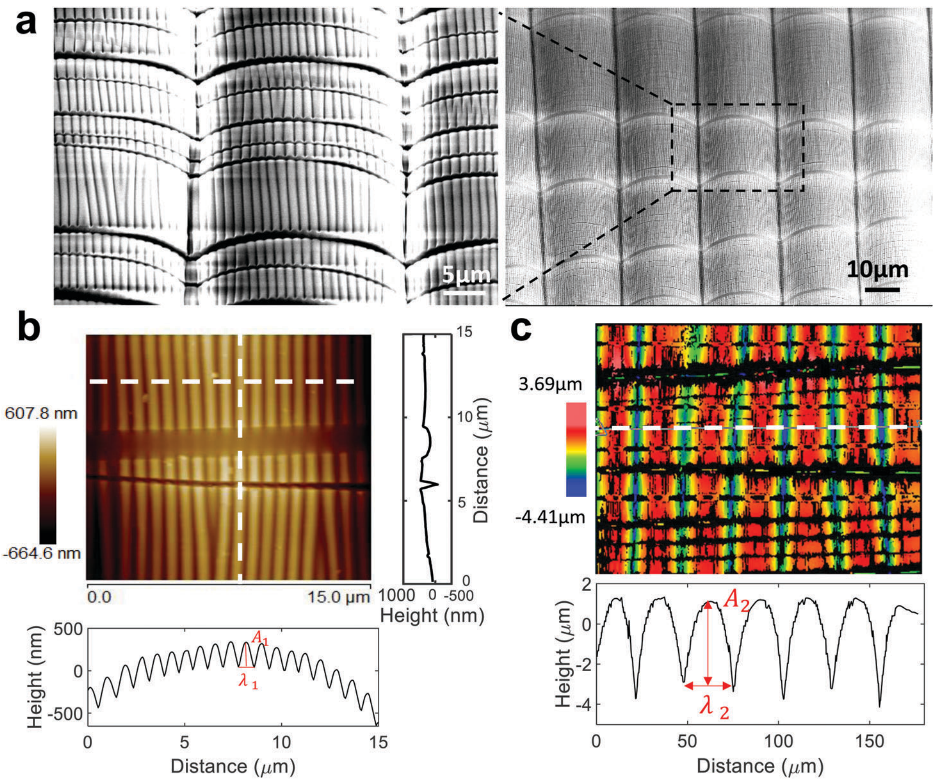


Fig. 2 (a) SEM images of hierarchical wrinkles generated with $\varepsilon_1 = \varepsilon_2 = 25\%$, $T_1 = 5$ min, $T_2 = 40$ min. Left: Magnified view. (b) Corresponding AFM images of hierarchical wrinkles with measured horizontal and vertical cross-sectional profiles along the white dashed line shown to the bottom and to the right, respectively. (c) Corresponding optical profilometer images of level-2 large-wavelength wrinkles in the hierarchical wrinkle with measured cross-sectional profile along the white dashed line shown to the bottom.

for small-wavelength wrinkles generated in the 1st step of plasma treatment, and $\lambda_2 \approx 15$–$35$ μm and $A_2 \approx 3.5$–$5.0$ μm for large-wavelength wrinkles generated in the 2nd step of UVO treatment. Generally, the wavelength and amplitude of wrinkles generated in either treatment step show an approximately linear relation with the treatment duration.

Meanwhile, a quantitative evaluation of the film thickness can be approximately obtained from eqn (1) with the measured wrinkle wavelength, *i.e.*

$$t_f = \frac{\lambda}{2\pi}\left(\frac{3\bar{E}_{sub}}{\bar{E}_f}\right)^{\frac{1}{3}} \tag{4}$$

The corresponding estimated film thickness as a function of treatment time is shown in Fig. S1 (ESI†), where literature values[39–41] for the mechanical properties of stiff silica layer generated by plasma treatment with $\bar{E}_f = 140$ GPa ($E_f = 130$ GPa and $\nu = 0.27$) and silica layer generated by UVO treatment with $\bar{E}_f = 43$ GPa ($E_f = 40$ GPa and $\nu = 0.27$), and $\bar{E}_{sub} = 2.3$ MPa ($E_{sub} = 1.8$ MPa and $\nu = 0.48$) for the PDMS substrate were used in eqn (4). It is found that the first layer of stiff films generated during plasma treatment has an approximate thickness $t_{f1}$ of 4–9 nm, while the second layer of stiff films generated during UVO treatment has an approximate thickness $t_{f2}$ of 150–350 nm, which is about 35 times thicker than the first layer. Since $t_{f2}$ is much larger than $t_{f1}$, the existence of level-1 small-wavelength wrinkles generated in the 1st step is expected to have a negligible effect on the dimension of level-2 large-wavelength wrinkles formed in the following step. This is confirmed by Fig. 3b, where given the measurement error, the change of the first stiff layer thickness with different treatment time $T_1$ almost does not affect the wavelength of level-2 wrinkles $\lambda_2$ generated in the 2nd step treatment.

### 3.2 Cracks in hierarchical wrinkles

Fig. 2b shows that two types of cracks with different depths and widths are also observed from the AFM-measured vertical cross section profile, the direction of which is orthogonal to the generated hierarchical wrinkles. This is due to the lateral tensile deformation resulting from the Poisson's effect, where cracks were generated during the strain release in both sequential steps. We believe that the shallow but wide crack with depth $\approx$ 200 nm and width $\approx$ 1.8 μm corresponds to the thinner stiff layer generated in the 1st step of plasma treatment. This is evidenced by the AFM measured cross-sectional profile cut from the valley of wrinkles (see Fig. 2b and Fig. S2, ESI†), where the wide crack vanished in the cross-sectional profile of the valleys, indicating that this is the first layer crack. The relatively deeper and narrower crack with depth $\approx$ 520 nm and width $\approx$ 0.7 μm corresponds to the thick stiff layer generated in the 2nd step of UVO treatment. The reason for the observed wider cracks during the 1st step release is that the subsequent applied strain during

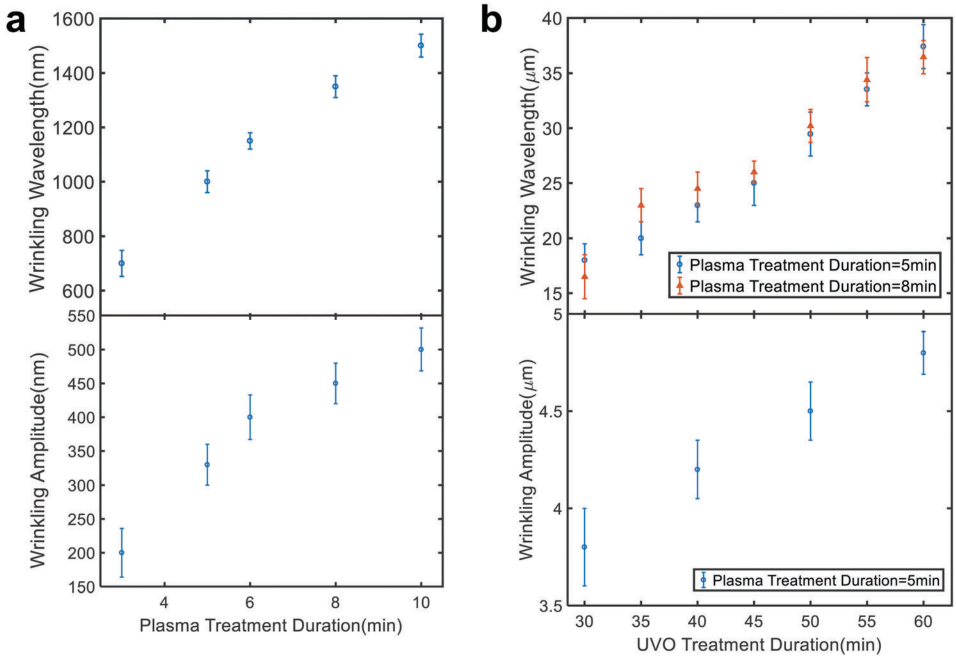


Fig. 3 (a) Measured wavelength and amplitude of the generated small-wavelength wrinkles as a function of the plasma treatment duration. (b) Measured wavelength and amplitude of the generated large-wavelength wrinkles as a function of the UVO treatment duration. All the pre-strain is set to be 25%.

the 2nd step release will further widen the cracks generated in the 1st step.

To quantify the relationship between the crack density and the change of the released strain and treatment time, we did a statistical study on the crack distribution by counting the number of cracks and analyzing the crack densities (defined as the number of cracks per 100 μm). The related result is shown in Fig. 4. Generally, upon strain release, the density of cracks generated during the 1st step of plasma treatment is much smaller than that of cracks generated during the 2nd step of the UVO treatment (Fig. 4). The reason is that the stiff film created by the UVO treatment is much thicker than that created by the plasma treatment (Fig. S1, ESI†), thus more prone to fracture. By varying the released strain in one step while fixing the released strain in the other, we found that the density of cracks generated during either step only depends on the released strain in its respective step (Fig. 4a and b). When we increased the plasma treatment duration, it shows a slight increase in the density of cracks upon strain release in both steps (Fig. 4c). However, it was found that longer UVO treatment duration will only increase the density of cracks generated in the 2nd-step strain release (Fig. 4d). In general, we found that similar to the formation of wrinkles, the cracks generated from the 1st and 2nd step strain release are independent of each other, and the crack density is more sensitive to the released strain than the plasma-UVO treatment time.

### 3.3 Effect of wrinkles' dimension on anisotropic wetting behavior of hierarchical wrinkled surfaces

Equipped with the knowledge of controlling the geometrical size of hierarchical wrinkles, next we investigated how the hierarchical dimension influences their corresponding anisotropic wetting behavior.

Fig. 5a shows the representative anisotropic wetting behavior of a 5 μL water droplet on a hierarchical wrinkled surface with $A_1 \approx 267$ nm, $\lambda_1 \approx 750$ nm, and $A_2 \approx 4.2$ μm, $\lambda_2 \approx 21.4$ μm. The droplet size is small such that the effect of its gravitational force can be negligible. The top view of the water droplet shows that the water droplet became elongated along the wrinkle grooves. The apparent static contact angles were measured along both perpendicular and parallel directions to the orientation of wrinkles (Fig. 5b). The parallel direction's contact angles $\theta_{\text{parallel}}$ along the wrinkles were 4 degrees larger than those measured from the perpendicular direction to the wrinkles $\theta_{\text{perpendicular}}$, indicating an anisotropic wetting behavior on the hierarchical wrinkled surface. The value of the wetting anisotropy $\Delta\theta$ is defined as the difference of the contact angles measured from these two orthogonal directions,[42] *i.e.*

$$\Delta\theta = \theta_{\text{parallel}} - \theta_{\text{perpendicular}} \tag{5}$$

By tuning the amplitude and wavelength of micro-wrinkles, we studied the effect of the aspect ratio of level-2 wrinkles (which is defined as $A_2/\lambda_2$) on the contact angle values and degree of wetting anisotropy of the hierarchical wrinkled surfaces, while the size of level-1 sub-micron wrinkles is approximately kept as the same ($A_1 \approx 300$ nm, $\lambda_1 \approx 800$ nm) considering the experimental measurement error. The results of the measured static contact angles along with dynamic contact angles in both directions are summarized in Table 1. We find that as the aspect ratio $A_2/\lambda_2$ grows from 0.024 to 0.128, $\theta_{\text{parallel}}$ increases from 112° to 120°, while $\theta_{\text{perpendicular}}$ remains almost unchanged with a value of about 110°. Meanwhile, the degree of wetting

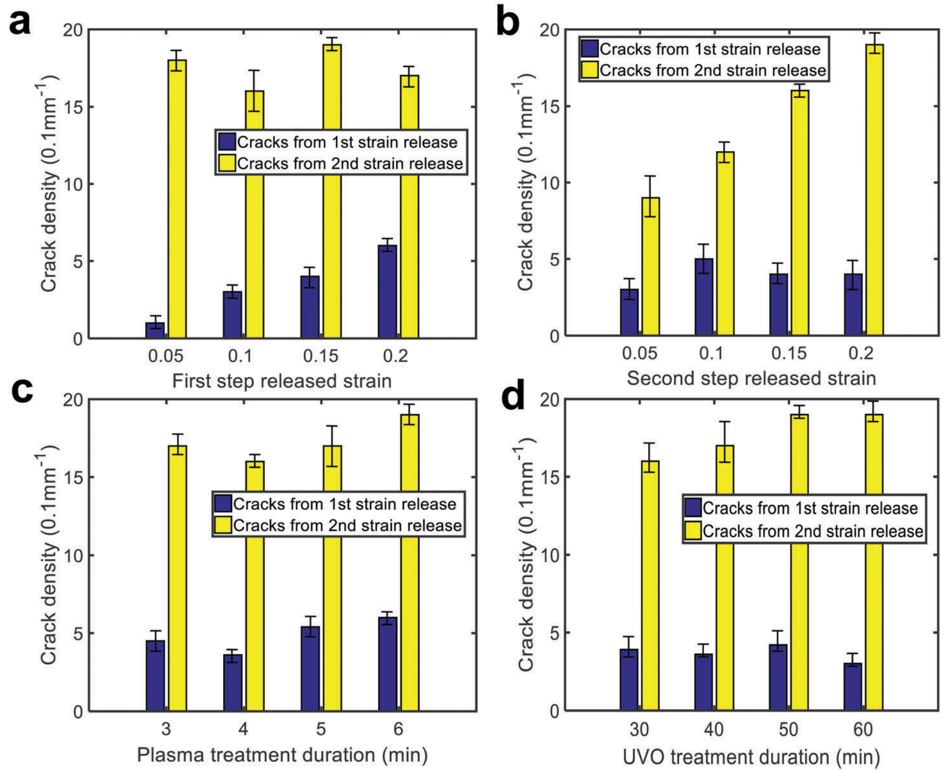


Fig. 4 Dependence of the measured crack densities on (a) 1st-step released strain, (b) 2nd-step released strain, (c) plasma treatment duration, and (d) UVO treatment duration.

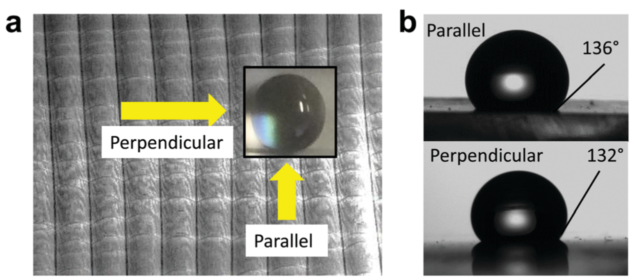


Fig. 5 (a) SEM image of a hierarchical wrinkled structure with $A_1 \approx 267$ nm, $\lambda_1 \approx 750$ nm, $A_2 \approx 4.2$ μm, $\lambda_2 \approx 21.4$ μm. Inset: Top view optical image of a 5 μL water droplet resting on the hierarchical wrinkled surface. (b) Side views of the droplet oriented to the parallel (top) and perpendicular (bottom) directions of wrinkles, respectively.

anisotropy $\Delta\theta$ increases from 3° to 9°. When the aspect ratio is further increased, *i.e.* $0.13 < A_2/\lambda_2 < 0.2$, both $\theta_{\text{parallel}}$ and $\theta_{\text{perpendicular}}$ reach 125°–135° and $\Delta\theta$ becomes about 4°–5°.

We further notice that as $A_2/\lambda_2$ increases, along the parallel direction, the advancing contact angles increase from 115° to 140° while the receding contact angles decrease from 75° to 66°. A similar trend was also observed for the advancing and receding contact angles along the perpendicular direction. The contact angle hysteresis of both parallel and perpendicular directions increases with the growing aspect ratios of level-2 micro-wrinkles. However, the contact angle hysteresis along the parallel direction is larger than that along the perpendicular direction for all aspect ratios ranging from 0.024 to 0.196, indicating that the water droplet is easier to transport along the perpendicular direction.

The increase in the degree of wetting anisotropy with the wrinkle aspect ratio in hierarchical wrinkles is consistent with the observation on single-period micro-wrinkles generated through UVO treatment on pre-strained PDMS substrate reported by Chung *et al.*[33] However, in sharp contrast to their reported large value of wetting anisotropy ($\Delta\theta$ up to 50°) in single-period wrinkles,[33] the self-similar hierarchical wrinkles in this work show a much smaller $\Delta\theta$ of up to 10°. Similar small degree of wetting anisotropy is also reported by Lee *et al.*,[43] on superhydrophobic non-similar hierarchical wrinkled surfaces, which are generated by depositing layer-by-layer silica nanoparticles on single-period micro-wrinkled PDMS substrate through UVO treatment. They found that as the surface roughness of hierarchical nanostructures increases, the wettability can even transit from anisotropic ($\Delta\theta \approx 18°$, hydrophobic wetting state) to isotropic wetting ($\Delta\theta \approx 0°$, superhydrophobic wetting state) despite the existence of anisotropic micro-wrinkled microstructures.[43] After comparing the wettability on different structured wrinkled PDMS substrates including single-period micro-wrinkles (static CAs in the range of 64°–100°),[33] self-similar multiscale hierarchical wrinkles (static CAs in the range of 110°–135°, this work), and nanoparticles on single-period micro-wrinkles (static CAs in the range of 110°–175°),[43] it suggests that the observed reduced degree of wetting anisotropy in the hierarchical wrinkles be partially attributed to the increased hydrophobicity due to the hierarchical nanostructures.

 

Table 1 Measured static and dynamic contact angles and degrees of wetting anisotropy on hierarchical wrinkled PDMS substrate

| | | | | | | Parallel | | | Perpendicular | | | |
|---|---|---|---|---|---|---|---|---|---|---|---|---|
| $A_1$ (nm) | $\lambda_1$ (nm) | $A_2$ (μm) | $\lambda_2$ (μm) | $A_2/\lambda_2$ | Crack densities (0.1 mm$^{-1}$) | Stat. (deg) | Adv. (deg) | Rec. (deg) | Stat. (deg) | Adv. (deg) | Rec. (deg) | $\Delta\theta$ (deg) |
| 275 | 822 | 0.6 | 25 | 0.024 | 4/8 | 112 | 115 | 75 | 109 | 120 | 93 | 3 |
| 322 | 774 | 2.75 | 39 | 0.071 | 6/12 | 113 | 116 | 74 | 110 | 121 | 90 | 3 |
| 305 | 790 | 3.5 | 39 | 0.090 | 4/10 | 115 | 118 | 73 | 110 | 119 | 87 | 5 |
| 311 | 825 | 4.35 | 34 | 0.128 | 4/14 | 120 | 122 | 75 | 111 | 118 | 89 | 9 |
| 247 | 770 | 2.5 | 16.7 | 0.150 | 3/15 | 129 | 134 | 72 | 125 | 129 | 82 | 4 |
| 297 | 800 | 4.5 | 25.8 | 0.174 | 4/17 | 127 | 131 | 62 | 124 | 130 | 87 | 3 |
| 270 | 776 | 3.75 | 20 | 0.188 | 5/20 | 135 | 136 | 64 | 130 | 133 | 85 | 5 |
| 315 | 815 | 4.5 | 23.3 | 0.193 | 7/18 | 134 | 138 | 68 | 129 | 134 | 82 | 5 |
| 267 | 750 | 4.2 | 21.4 | 0.196 | 5/21 | 136 | 140 | 66 | 132 | 137 | 84 | 4 |

Under superhydrophobic cases, anisotropic wetting could be largely suppressed by the superhydrophobicity of patterned surfaces, as evidenced by the observed small angle of wetting anisotropy in a multiscale hierarchical rice leaf surface ($\theta_{\text{parallel}} \approx 154^\circ$ and $\theta_{\text{perpendicular}} \approx 157^\circ$ with $\Delta\theta \approx 3^\circ$) despite the anisotropic grooved microstructures.[43]

### 3.4 Wetting state of hierarchical wrinkles: theoretical analysis and experimental examination

Two classic wetting models, the Wenzel model and Cassie–Baxter (CB) models, are widely used to characterize the apparent contact angle on a rough surface.[30,44,45] The Wenzel model assumes that the surface is fully wetted, and its apparent contact angle $\theta^*$ will be enhanced by the surface roughness according to the equation:[46]

$$\cos\theta^* = r\cos\theta_Y \tag{6}$$

where $r$ is the surface roughness, and $\theta_Y$ is the Young contact angle of the material. The CB model, on the other hand, assumed that the air is trapped below the droplet forming a composite interface. The droplet wets in the CB wetting state follows the following equation:[47]

$$\cos\theta^* = f(1 + \cos\theta_Y) - 1 \tag{7}$$

where $f$ is the fraction of the projection area that is wet.

Regarding the wetting state in a sinusoidal-wave-like surface, Johnson and Dettre[48] demonstrated that for a single-period sinusoidal surface without hierarchy, the preferred wetting state could transfer from the Wenzel state to CB state when the aspect ratio is above a certain value. Bittoun *et al.*[36] showed the theoretical possibility of the CB state in a hierarchical sinusoidal structured surface.

To determine the wetting state on our hierarchical sinusoidal wrinkling surface, we theoretically calculated the surface free energy by following the thermodynamic model proposed by Marmur *et al.*[36,44] For a water droplet at a penetration depth $h$ ($0 < h < 1$) defined as the normalized distance between the liquid level and base (inset of Fig. 6a), the dimensionless surface free energy $G^*$ could be calculated as

$$G^* = F^{-\frac{2}{3}}(\theta)(2 - 2\cos\theta - (r_f f\cos\theta_Y + f - 1)\sin^2\theta) \tag{8}$$

where

$$F(\theta) = (2 - 3\cos\theta + \cos^3\theta) \tag{9}$$

where $r_f$ is the roughness ratio of the actual wet area and $\theta$ is the apparent contact angle. Both $r_f$ and $f$ are functions of the normalized droplet penetration depth $h$ ($0 < h < 1$), *i.e.* $r_f = r_f(h)$, $f = f(h)$. It is known that among all the apparent contact angles, the CB contact angle defined by eqn (7) (note that the CB contact angle will transfer to the Wenzel contact angle when it is fully penetrated) is associated with the lowest surface free energy.[36] Thus, by replacing $\theta$ with $\theta_{CB}$ in eqn (8), it could be further simplified as the following with only one argument $h$ left, *i.e.*

$$G^* = F^{-\frac{2}{3}}(\theta_{CB})(2 - 2\cos\theta_{CB} - (r_f f\cos\theta_Y + f - 1)\sin^2\theta_{CB}) \tag{10}$$

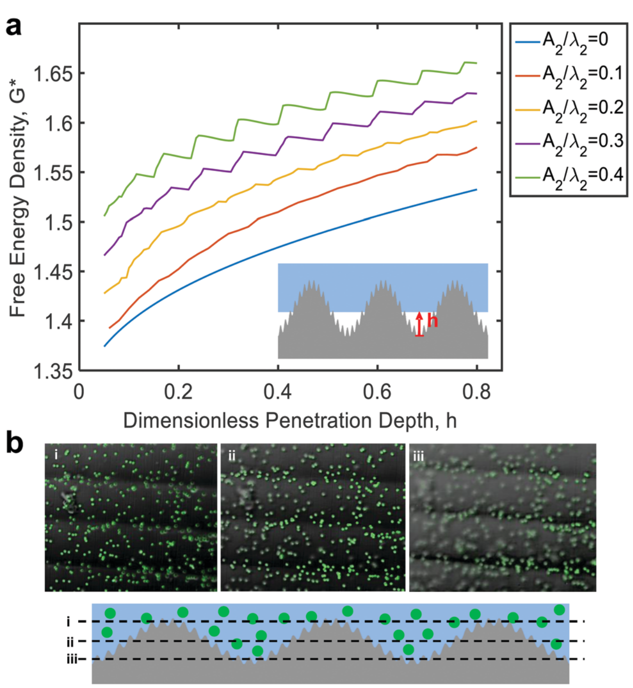


Fig. 6 (a) Dimensionless free energy density curves *vs.* the normalized penetration depth for hierarchical wrinkles with different wrinkling aspect ratios. Note that the curves have been translated vertically for clarity. (b) Confocal images combined with reflectance scan (grey) and fluorescence signal (green) at different focus lengths on the peak (i), middle (ii), and valley (iii) of the wrinkle grooves as illustrated by the schematic on the bottom. Nanoparticles (green) are seen from the peaks to the valleys of the wrinkles. The hierarchical wrinkled structure has the dimension of $A_1 \approx 267$ nm, $\lambda_1 \approx 750$ nm, $A_2 \approx 4.2$ μm, $\lambda_2 \approx 21.4$ μm.

The minimums of eqn (10) must also be the minimums of original eqn (8).

For the observed hierarchical sinusoidal wrinkles, their geometrical profiles can be modelled by:

$$y = A_1 \sin\left(\frac{\pi}{\lambda_1}x\right)^2 + A_2 \sin\left(\frac{\pi}{\lambda_2}x\right)^2 \tag{11}$$

A Matlab code was developed to numerically calculate $r_f$ and $f$ in eqn (10) for the hierarchical surface morphology modeled by eqn (11), where normalized droplet penetration depth $h$ varied from 0 to 1 in incremental steps of 0.01. For the calculation, the Young contact angle is chosen as the measured value of $\theta_Y = 96^\circ$ for the treated PDMS substrate without pre-stretching or wrinkle, which shows slight hydrophobicity, as well as isotropic wettability in both parallel and perpendicular directions. Due to cracks-induced accelerated hydrophobic recovery,[49] our measured Young CA is larger than the previously reported data in literature.[33] In addition, the amplitude and wavelength of level-1 wrinkles used in the calculations were fixed by taking the same value as those in experiments with $A_1$ = 300 nm, $\lambda_1$ = 800 nm.

In Fig. 6a, we plot the calculated free energy density *versus* the penetration depth $h$ for the hierarchical wrinkled surface with different aspect ratios of level-2 micro-wrinkles (*i.e.* $A_2/\lambda_2$ = 0, 0.1, 0.2, 0.3, and 0.4). For relatively shallow micro-wrinkles with $A_2/\lambda_2 \leq 0.2$, the regime that our samples locate, the free energy density has one single minimum at $h = 0$, which means that the droplet penetrates into the grooves of wrinkles and fully wets the surface, corresponding to a Wenzel state. That is to say, our hierarchical wrinkled samples with aspect ratios of no larger than 0.2 all favor a Wenzel wetting state. As $A_2/\lambda_2$ further increases, *i.e.* $0.2 < A_2/\lambda_2 \leq 0.4$, we notice that unlike the low-aspect-ratio hierarchical wrinkles, in this case the free energy density has multiple local minima at various penetration depths. These local minima represent the metastable CB states. However, the Wenzel state at $h = 0$ is still the most stable wetting state associated with the lowest free energy density. Therefore, we validate that the hierarchical wrinkled surfaces do have the theoretical possibility to support the CB state as predicted by Bittoun *et al.*[36] but it requires a much higher aspect ratio of $A_2/\lambda_2$ = 0.3–0.4. However, to date the aspect ratio of most reported wrinkles generated in experiments is limited to be lower than 0.3 due to the transition to localized modes such as creasing,[50–52] folding,[53–55] ridging,[19,56,57] and period-doubling,[55,58] thus making it hard to transit to CB states.

To further examine the theoretically predicted wetting state, we used the fluorescent particle dispersed water and confocal microscopy to capture the penetration depth that water droplets wet the wrinkle grooves by following the technique introduced by Verho[59] (see Experimental section for information). A 5 μL droplet of fluorescence marked particles dispersed water was gently deposited on the sample surface with $A_1$ = 267 nm, $\lambda_1$ = 750 nm, $A_2$ = 4.2 μm, $\lambda_2$ = 21.4 μm, which has the largest aspect ratio of $A_2/\lambda_2 \approx 0.2$ in Table 1. As illustrated in the schematic (bottom of Fig. 6b), the confocal microscope was set to focus on the peak (i), middle (ii), and valley (iii) of the wrinkling grooves. A 488 nm laser was used to excite the fluorescence. Two signals could be received from the observation. The conventional reflectivity signals show the surface structure and the fluorescence signal indicates the distribution of water. Due to the limit of the resolution, the level-1 sub-micron wrinkles were not able to be observed.

Fig. 6b shows the corresponding fluorescent images at the three representative depths. At position (i), *i.e.* the peak of wrinkles, all the fluorescent micro-particles at this layer were excited (Fig. 6b(i)), showing no concentration of water. At position (ii), *i.e.* the middle of wrinkles, the fluorescent micro-particles at the side walls of wrinkle grooves became lit, indicating the presence of water in those regions (Fig. 6b(ii)). At position (iii), *i.e.* the valley of wrinkle grooves, the fluorescent micro-particles in a narrow region emitted lights, showing that the water went all the way down to the bottom of the wrinkled structure (Fig. 6b(iii)). This confirms that the wetting state is the Wenzel state. Noting that in Fig. 6b(iii), since the confocal microscope focused on the valley of wrinkle grooves, the wrinkled structure cannot be seen very clear due to the small depth of the field of view of the objective.

### 3.5 Anisotropic wetting behavior of hierarchical wrinkles: theoretical analysis and experimental examination

Knowing that the wetting state of the hierarchical wrinkled samples is in the Wenzel state, we first plot the measured contact angles *versus* the aspect ratio of level-2 micro-wrinkles together with those predicted by the Wenzel model eqn (6) for comparison. The geometric parameters for level-1 sub-micron wrinkles are fixed as $A_1$ = 300 nm and $\lambda_1$ = 800 nm during all the calculations. As shown in Fig. S3 (ESI†), the predicted contact angle from the Wenzel model has a value of $\sim 100^\circ$ and shows a slight increase with the aspect ratio of the level-2 micro-wrinkles $A_2/\lambda_2$, due to the fact that the surface roughness does not change too much when tuning level-2 micro-wrinkles' aspect ratios in the range from 0 to 0.2 with the existence of level-1 sub-micron wrinkles. By comparing the value of the measured contact angles with that of the theoretically predicted contact angles, we found that the measured contact angles in both parallel and perpendicular directions deviated from the theoretical curve predicted by the Wenzel model with a difference in a range of 10%–30%. It could be seen that the Wenzel model is not able to predict the observed contact angles even when the wetting state is in the Wenzel state.

The failure of using the Wenzel model to predict the measured contact angle can be well explained from a dynamic point of view. Theoretically, the static contact angle could be an arbitrary value between advancing contact angle and receding contact angle depending on history. In our experiments, the static contact angles are close to the advancing contact angles because the water droplets are deposited in a way to increase the droplet volume (Table 1). Therefore, the larger static contact angles than the Wenzel contact angles here imply that the dynamic effect is involved in the wetting process. We decomposed the surface morphology into combined wrinkles and cracks which are orthogonal to each other, and then analyzed the three-phase contact line (TPCL) motion towards these two directions

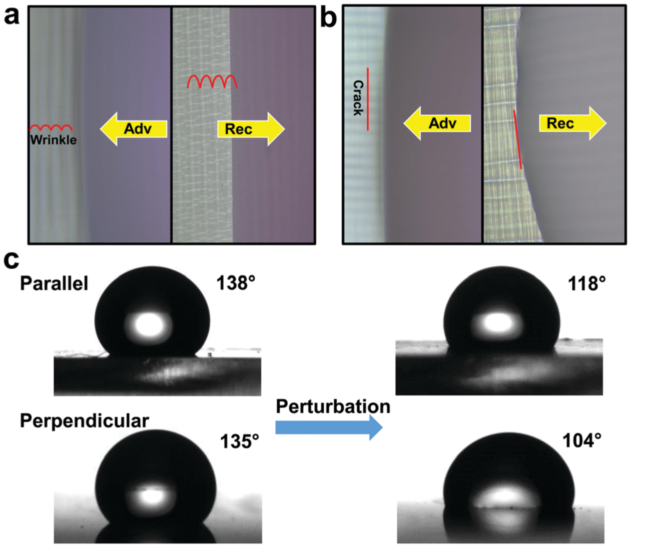


Fig. 7 Images of advancing and receding contact line when (a) contact line moves against hierarchical wrinkles (b) contact line moves against cracks. (c) Contact angles in the parallel and perpendicular directions of wrinkles before and after vibration on hierarchical wrinkled surfaces.

independently. When the TPCL moves against the wrinkles during the wetting and de-wetting process, it will pin on the wrinkle peaks as evidenced by the observed advancing and receding TPCL through optical microscopy (Fig. 7a). Note that the advancing TPCL cannot be observed directly due to the larger advancing contact angle than 90°. By observing the shape of the droplet, we find that the droplet has a straight contour, implying that the advancing TPCL is pinned and is straight (left of Fig. 7a). The receding TPCL is straight along the peak of wrinkles and shows more obvious pinning effect of the TPCL (right of Fig. 7a). Such a pinning effect blocks the motion of the TPCL, and it will induce an energy barrier to prevent the total energy of the system from decreasing to the minimum. A pinned advancing (receding) TPCL will lead to a larger (smaller) contact angle when compared with the equilibrium contact angle. Further adding (withdrawing) water will provide the water droplet additional energy to overcome the energy barrier, thus depin the TPCL and decrease (increase) the contact angle.

To validate the pinning and depinning effect, we provide the water droplet certain external energy through vibration. Such external energy will help the TPCL to overcome more energy barriers, thus leading to a decreased contact angle (top of Fig. 7c). When the sample was gently shaken (see experimental method for details), a sudden collapse of the water droplet was observed, where the contact angle decreased from 138° to 115°. Similar phenomenon was also observed when TPCL moves along the wrinkles (against cracks). The cracks will pin the advancing (receding) TPCL (Fig. 7b), leading to a larger (smaller) contact angle in the perpendicular direction when compared to the equilibrium contact angle. After the vibration perturbation, a sudden drop of the perpendicular contact angle from 135° to 104° was also observed (bottom of Fig. 7c). Now we can conclude that the measured parallel and perpendicular contact angles which are larger than the Wenzel contact angle result from the pinning effect of wrinkles and cracks, respectively.

To better understand the physics of the pinning and depinning shown in Fig. 7, a thermodynamic calculation of the change in the surface free energy during the TPCL moving against the wrinkles was performed. Modeling of the water droplet moving against the wrinkles was illustrated in Fig. 8. In this model, a position with the apparent contact angle of 90° is set to be a reference where the free energy is 0 and $x$-coordinate is 0. The total free energy change ($\Delta G$) due to the movement of the TPCL to a new position $x$ with respect to the reference point 0 is represented by

$$\Delta G = \int_0^x -\gamma_{\mathrm{lv}} \cos\theta_{\mathrm{Y}} \sqrt{1 + \left(\frac{\mathrm{d}y}{\mathrm{d}x}\right)^2}\,\mathrm{d}x + \gamma_{\mathrm{lv}}\Delta H \tag{12}$$

where $\gamma_{\mathrm{lv}}$ is the liquid–vapor interfacial tension, $y(x)$ is the hierarchical wrinkle profile represented by eqn (11), $\Delta H$ is the change in the length of liquid–vapor interface. The left term in eqn (12) calculates the interfacial energy change resulting from the replacement of a solid–vapor interface by a solid–liquid interface. The right term is the interfacial energy change caused by the change in the length of liquid–vapor interface. The effect of gravity is neglected here. Since $\Delta H$ cannot be determined exactly, here we adopt the concept of liquid front for an approximation.[60] In general, as the size of a water droplet is much larger than the characteristic scale of wrinkles, a small portion of the liquid–vapor interface near the solid surface could be approximated as a straight line with a length $H_0$ and a contact angle $\theta$. After the TPCL moves a small distance $x$, the liquid front changes to a state with a length $H$ and a contact angle of $\theta + \Delta\theta$. Thus $\Delta H$ could be estimated as

$$\Delta H = H - H_0 = \sqrt{(H_0 - y)^2 + x^2} - H_0 \tag{13}$$

The relationship between $H_0$ and contact angle $\theta$ could be obtained by a geometric relation:

$$\tan\theta = \frac{H_0 - y}{x} \tag{14}$$

Based on eqn (12)–(14), a Matlab code was programmed to numerically calculate the free energy change with respect to the apparent contact angle. In all the calculations, we set $\gamma_{\mathrm{lv}}$ = 72.6 mJ m$^{-2}$ (water surface tension in room temperature), $H_0$ = 200 μm. The chosen $H_0$ is much larger than the scale of wrinkles. In fact, it is found that the $\Delta G$ *vs.* $\theta$ curve is independent of $H_0$.[60]

For a hierarchical wrinkled surface with $A_1$ = 267 nm, $\lambda_1$ = 750 nm, $A_2$ = 4.2 μm, $\lambda_2$ = 21.4 μm, the $\Delta G$–$\theta$ curve in Fig. 9a shows a number of local minima, which represent the energy barriers. The local extremes exist at two scales, indicating that in our hierarchical wrinkled surface, both level-1 and level-2 wrinkles will provide the energy barriers and pin the TPCL. The small energy barriers correspond to the level-1 sub-micron wrinkles while the large energy barriers correspond to the level-2 micro-wrinkles. To overcome the energy barrier from the level-1 and level-2 wrinkles, the energy needed is 0.2 μJ and 4 μJ, respectively, indicating that it will take 20 times more energy to overcome a large energy barrier than that required to

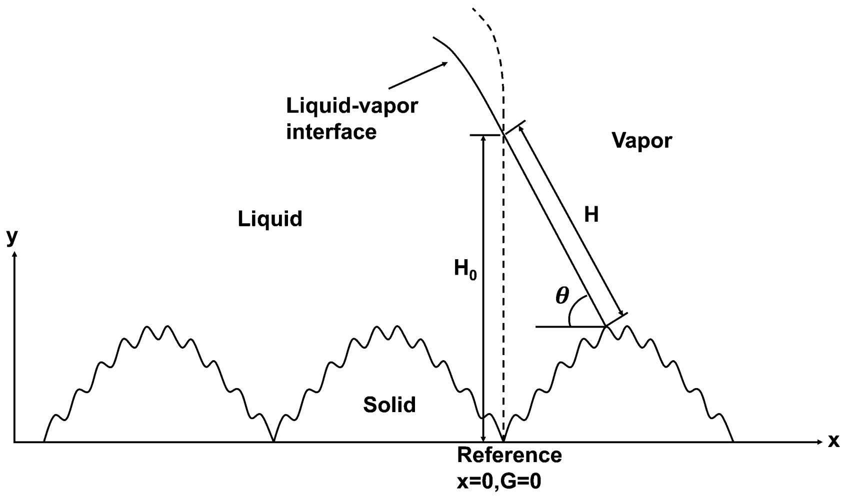


Fig. 8 Schematic model for the three-phase contact line moving against hierarchical wrinkled structure.

overcome a small energy barrier. Theoretically, the first and last local minimum in the $\Delta G$–$\theta$ curve correspond to two limiting angles, *i.e.* the receding contact angle $\theta_R$ and advancing contact angle $\theta_A$, which are $\theta_R = 46^\circ$ and $\theta_A = 149^\circ$ here (inset of Fig. 9a). However, since the level-2 micro-wrinkles are the major energy barriers, it is highly possible that the receding and advancing contact angles are mainly determined by the large energy barriers from the level-2 micro-wrinkles. With this assumption, by only counting the large energy barriers, now we can obtain a modified receding contact angle ($\theta_R{*} = 71^\circ$) and a modified advancing contact angle ($\theta_A{*} = 124^\circ$) from Fig. 9a. There is a global minimum of 99° corresponding to the Wenzel contact angle.

To investigate the effect of aspect ratio of the level-2 micro-wrinkles on the total free-energy change, we also plot the $\Delta G$–$\theta$ curves for hierarchical wrinkles with different $A_2/\lambda_2$ = 0.024, 0.090, 0.150, 0.196 together (Fig. 9b). As expected, the energy barriers from level-2 micro-wrinkles decrease dramatically with the reduced aspect ratio. When the aspect ratio is close to zero, the two scales of the energy barriers in the free energy curve are reduced to one. On contrast, the energy barriers from the level-1 sub-micron wrinkles remain almost unchanged due to their approximately constant aspect ratio (inset of Fig. 9b). Therefore, we can see that the magnitude of the energy barriers is dependent of the aspect ratio of the wrinkles. For hierarchical wrinkles with a larger aspect ratio, it can form deeper energy barriers, thus leading to a stronger pining effect.

To validate our theory, we compare the theoretically predicted advancing and receding contact angles with experimental measurements, the data of which are summarized in Table 2. Generally, we can see that as the aspect ratio of level-2 micro-wrinkles increases from 0.024 to 0.196, the calculated advancing contact angles increase while the calculated receding contact angles decrease. The unmodified advancing contact angles provide an upper limit as it counts the energy barriers from both hierarchical-level wrinkles, while the modified advancing contact angles provide a lower limit since only level-2 micro-wrinkles are considered to contribute to the energy barriers. Similarly, for the receding contact angles, the unmodified ones represent the lower limit while the modified ones represent the upper limit. Thus, the predicted unmodified and modified contact angles from the theory set the upper and lower limit for the possible values of a measured advancing/receding contact

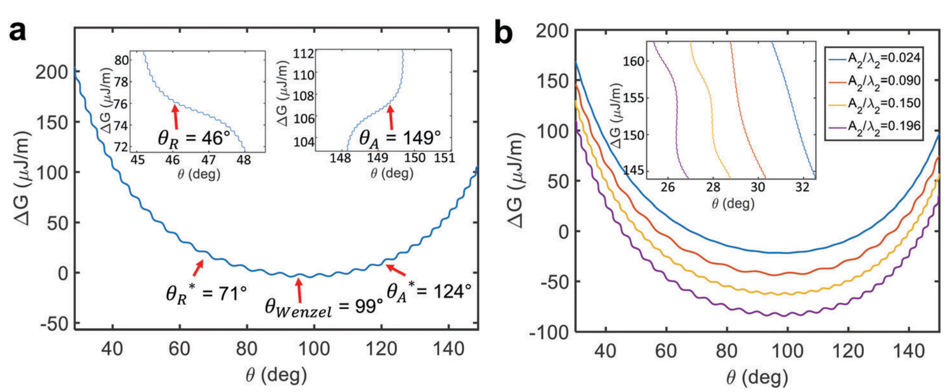


Fig. 9 (a) Free energy change as a function of contact angle when the three phase contact line moves against the wrinkles for the hierarchical wrinkled structure with $A_1 \approx 267$ nm, $\lambda_1 \approx 750$ nm, $A_2 \approx 4.2$ µm, $\lambda_2 \approx 21.4$ µm (b) Free energy changes as a function of contact angle when the three phase contact line moves against the wrinkles for the hierarchical wrinkled samples with different aspect ratios of level-2 micro-wrinkles.

 

angle in experiments. As shown in Table 2 on the comparison of both advancing and receding contact angle between experiment and theory, both the measured advancing and receding contact angles for all the hierarchical wrinkled samples with aspect ratio ranging from 0.024 to 0.196 fall into the range predicted by theory, validating our theoretical models.

### 3.6 Some remarks on anisotropic wetting resulting from the coexistence of orthogonal wrinkles and cracks

When a water droplet is deposited on the hierarchical wrinkled surface, it cannot automatically go to the position with the lowest free energy, *i.e.* the Wenzel contact angle, due to the existence of energy barriers. Instead, the TPCL will be trapped into a metastable state with a contact angle larger than the Wenzel contact angle. Only when enough energy is input, the TPCL can overcome the energy barriers and continue to move. Therefore, the observed apparent contact angles are the intermediate contact angle between the advancing contact angle and Wenzel contact angle as validated by the data in Table 2. Furthermore, when the TPCL moves along the wrinkles, it will encounter cracks. To estimate the influence of cracks, we did a quantitative analysis based on the statistical data of cracks densities and dimensions (see ESI† for details). From the SEM images shown in Fig. 1a, the average interval in between narrow cracks and in between wide cracks is approximately 6 μm and 33 μm, respectively. The depth of narrow cracks and wide cracks are estimated to be 520 nm and 200 nm, respectively. Based on these measured data, the surface roughness factor $r$ can be estimated to be $\sim$1.13 and the solid fraction $f$ is $\sim$86% due to the existence of cracks. Since the cracks-induced changes in surface roughness and solid fraction are small, the main effect of cracks lies in forming the energy barriers and pinning the TPCL in a way similar to the effect of wrinkles. In addition to the wrinkled surface morphology, the existence of cracks exposed the untreated PDMS, forming a chemical contrast with treated PDMS. Such heterogeneous chemical pattern will also lead to an anisotropic wetting[28] that will enhance the pinning effect of cracks.

For wrinkled surfaces without cracks, previous studies have shown that the perpendicular contact angle is close to the Young contact angle on a flat surface.[33,42] For our samples, the perpendicular contact angles are larger than the Young contact angle due to the pinning effect of cracks (Fig. 7b). Generally, the crack density increases with the aspect ratio of level-2 micro-wrinkles, thus leading to an increased density of energy barriers. Therefore, a sample surface with more cracks will have a larger perpendicular contact angle, as evidenced by the data shown in Table 1. That is to say, wrinkles and cracks will compete with each other in elongating the droplet along their respective orientation, which partially accounts for the observed small degrees of wetting anisotropy in experiments. Similar competition between two orthogonal features through imprinted hierarchical structures was reported by Zhang *et al.*[31] in determining the wetting anisotropy, where the smallest degree of wetting anisotropy was observed when the second level rectangular grooves are orthogonal to those in the first level with similar scales. Examples of competition between orthogonal features in determining the anisotropic wetting in hierarchical structured surfaces can also be observed in nature. Koch *et al.*[61] revealed that daisy florets have several different hierarchical structures, including parallel hemispherical protrusions with cuticle folds on top and perpendicular to the protrusions, parallel trapezoid protrusions with cuticle folds on top surface and parallel with protrusions, and parallel triangular protrusions with cuticle folds on side walls and perpendicular to protrusions.[61] Among these three anisotropic structures, the second one, *i.e.* the protrusions and cuticle folds have the same orientation, demonstrate the largest wetting anisotropy ($\Delta\theta \approx 46°$), while the other two structures exhibiting two orthogonal features have a much smaller wetting anisotropy ($\Delta\theta \approx 12°–17°$) due to the competing contact line pinning effect.

Another potential contribution factor to the small degree of wetting anisotropy in the hierarchical wrinkled PDMS samples could be the hydrophobicity of PDMS materials itself. Previous research has shown that the hydrophobicity of materials could also reduce the anisotropy of wetting,[62] especially when the hydrophobicity of the materials is high enough to enable the formation of CB state on certain anisotropic structured surface, the wetting on such surfaces could be nearly isotropic. In our case, the hydrophobicity is expected to reduce the wetting anisotropy but within a very limited extent since the wetting state in hierarchical wrinkles is still Wenzel state. Thus, we believe that the pinning effect plays a dominant role in determining the observed small degree of wetting anisotropy.

Table 2 Calculated and measured advancing and receding contact angles in the parallel direction of hierarchical wrinkled PDMS substrate

| | | | | | | | Adv. (deg) | | | Rec. (deg) | | |
|---|---|---|---|---|---|---|---|---|---|---|---|---|
| $A_1$ (nm) | $\lambda_1$ (nm) | $A_2$ (μm) | $\lambda_2$ (μm) | $A_2/\lambda_2$ | Static (deg) | Wenzel (deg) | Expt | Calcd[a] | Calcd | Expt | Calcd[a] | Calcd |
| 275 | 822 | 0.6 | 25 | 0.024 | 112 | 97.8 | 115 | 106 | 132 | 75 | 93 | 62 |
| 322 | 774 | 2.75 | 39 | 0.071 | 113 | 98.6 | 116 | 105 | 140 | 74 | 85 | 57 |
| 305 | 790 | 3.5 | 39 | 0.090 | 115 | 98.5 | 118 | 107 | 140 | 73 | 86 | 52 |
| 311 | 825 | 4.35 | 34 | 0.128 | 120 | 98.3 | 122 | 112 | 144 | 75 | 80 | 49 |
| 247 | 770 | 2.5 | 16.7 | 0.150 | 129 | 97.8 | 134 | 114 | 144 | 72 | 79 | 50 |
| 297 | 800 | 4.5 | 25.8 | 0.174 | 127 | 98.5 | 131 | 119 | 145 | 62 | 76 | 45 |
| 270 | 776 | 3.75 | 20 | 0.188 | 135 | 98.3 | 136 | 123 | 147 | 64 | 76 | 45 |
| 315 | 815 | 4.5 | 23.3 | 0.193 | 134 | 98.9 | 138 | 124 | 148 | 68 | 75 | 44 |
| 267 | 750 | 4.2 | 21.4 | 0.196 | 136 | 98.4 | 140 | 124 | 149 | 66 | 71 | 46 |

[a] Represents modified advancing or receding contact angles.

# 4. Conclusions

In summary, we studied the anisotropic wetting behavior on self-similar hierarchical wrinkled surfaces through a combined experimental characterization and theoretical modeling. The hierarchical wrinkled surface with features crossing from hundreds of nanometers to tens of microns is fabricated through sequential plasma and UVO treatment upon sequential strain release. The dimension of wrinkles at each hierarchical level can be quantitatively and independently controlled by manipulating the treatment time and sequential strain release. The hierarchical dimensional effect on the wetting state and anisotropic wetting behavior of the hierarchical wrinkled surfaces was systematically investigated through both experimental and theoretical analysis. We concluded that the observed apparent contact angles are the intermediate contact angles between the advancing contact angles and the Wenzel contact angles due to the energy barriers from orthogonal wrinkles and cracks, which is validated by both experiments and theoretical predictions. Furthermore, the competition between orthogonal wrinkles and cracks in contact line pinning accounts for the observed small degree of wetting anisotropy in the hierarchical wrinkled surfaces.

We noted that the mechanism of anisotropic wettability on hierarchical structures is still not well understood, where the exact wetting state at nanoscale remains unknown. As noted by Rahmawan *et al.*,[63] there are four possible combinations of wetting state in a dual roughness surface: both the wetting state of microscale and nanoscale are Wenzel ($W^m$–$W^n$); the microscale wetting state is Wenzel but the nanoscale wetting state is CB ($W^m$–$C^n$); both microscale and nanoscale wetting states are CB ($C^m$–$C^n$); and the microscale wetting state is CB while the nanoscale wetting state is Wenzel ($C^m$–$W^n$). Due to the limited knowledge of the wetting state on the nanoscale, here the use of Wenzel wetting state in both large scale and small scale represents a simplified explanation of its complex wetting behavior. The results of this work could find potential applications in microfluidics, antifouling, and waterproofing.

## Conflicts of interest

There are no conflicts of interest to declare.

## Acknowledgements

J. Y. acknowledges the funding support from the start-up at Temple University and National Science Foundation (NSF-CMMI-1745921). We thank the help from Mr Prashant Chandrasekaran and Dr Lin Han at Drexel University with the AFM measurement.

## References

1 W. Barthlott and C. Neinhuis, *Planta*, 1997, **202**, 1–8.
2 K. Autumn, Y. A. Liang, S. T. Hsieh, W. Zesch, W. P. Chan, T. W. Kenny, R. Fearing and R. J. Full, *Nature*, 2000, **405**, 681–685.
3 Z.-Z. Gu, H. Uetsuka, K. Takahashi, R. Nakajima, H. Onishi, A. Fujishima and O. Sato, *Angew. Chem., Int. Ed.*, 2003, **42**, 894–897.
4 K. Koch, B. Bhushan, Y. C. Jung and W. Barthlott, *Soft Matter*, 2009, **5**, 1386–1393.
5 B. Cortese, S. D'Amone, M. Manca, I. Viola, R. Cingolani and G. Gigli, *Langmuir*, 2008, **24**, 2712–2718.
6 Y. Lee, S. H. Park, K. B. Kim and J. K. Lee, *Adv. Mater.*, 2007, **19**, 2330–2335.
7 N. J. Shirtcliffe, G. McHale, M. I. Newton, G. Chabrol and C. C. Perry, *Adv. Mater.*, 2004, **16**, 1929–1932.
8 Y. Li, X. J. Huang, S. H. Heo, C. C. Li, Y. K. Choi, W. P. Cai and S. O. Cho, *Langmuir*, 2007, **23**, 2169–2174.
9 S. G. Lee, D. Y. Lee, H. S. Lim, D. H. Lee, S. Lee and K. Cho, *Adv. Mater.*, 2010, **22**, 5013–5017.
10 E. Lee, M. Zhang, Y. Cho, Y. Cui, J. Van der Spiegel, N. Engheta and S. Yang, *Adv. Mater.*, 2014, **26**, 4127–4133.
11 W. H. Koo, S. M. Jeong, F. Araoka, K. Ishikawa, S. Nishimura, T. Toyooka and H. Takezoe, *Nat. Photonics*, 2010, **4**, 222–226.
12 P. J. Yoo and H. H. Lee, *Langmuir*, 2008, **24**, 6897–6902.
13 H. S. Kim and A. J. Crosby, *Adv. Mater.*, 2011, **23**, 4188–4192.
14 E. P. Chan and A. J. Crosby, *Adv. Mater.*, 2006, **18**, 3238–3242.
15 C. M. Stafford, C. Harrison, K. L. Beers, A. Karim, E. J. Amis, M. R. VanLandingham, H.-C. Kim, W. Volksen, R. D. Miller and E. E. Simonyi, *Nat. Mater.*, 2004, **3**, 545–550.
16 A. Schweikart and A. Fery, *Microchim. Acta*, 2009, **165**, 249–263.
17 K. Efimenko, M. Rackaitis, E. Manias, A. Vaziri, L. Mahadevan and J. Genzer, *Nat. Mater.*, 2005, **4**, 293–297.
18 X. Yang, Y. Zhao, J. Xie, X. Han, J. Wang, C. Zong, H. Ji, J. Zhao, S. Jiang, Y. Cao and C. Lu, *ACS Nano*, 2016, **10**, 3801–3808.
19 C. Cao, H. F. Chan, J. Zang, K. W. Leong and X. Zhao, *Adv. Mater.*, 2014, **26**, 1763–1770.
20 P.-C. Lin and S. Yang, *Soft Matter*, 2009, **5**, 1011–1018.
21 R. Prathapan, J. D. Berry, A. Fery, G. Garnier and R. F. Tabor, *ACS Appl. Mater. Interfaces*, 2017, **9**, 15202–15211.
22 J. Yin, J. L. Yagüe, D. Eggenspieler, K. K. Gleason and M. C. Boyce, *Adv. Mater.*, 2012, **24**, 5441–5446.
23 G. Lin, P. Chandrasekaran, C. Lv, Q. Zhang, Y. Tang, L. Han and J. Yin, *ACS Appl. Mater. Interfaces*, 2017, **9**, 26510–26517.
24 L. Feng, S. Li, Y. Li, H. Li, L. Zhang, J. Zhai, Y. Song, B. Liu, L. Jiang and D. Zhu, *Adv. Mater.*, 2002, **14**, 1857–1860.
25 S. G. Lee, H. S. Lim, D. Y. Lee, D. Kwak and K. Cho, *Adv. Funct. Mater.*, 2013, **23**, 547–553.
26 A. Roth-Nebelsick, M. Ebner, T. Miranda, V. Gottschalk, D. Voigt, S. Gorb, T. Stegmaier, J. Sarsour, M. Linke and W. Konrad, *J. R. Soc., Interface*, 2012, **9**, 1965.
27 Y. Zheng, X. Gao and L. Jiang, *Soft Matter*, 2007, **3**, 178–182.
28 M. Morita, T. Koga, H. Otsuka and A. Takahara, *Langmuir*, 2005, **21**, 911–918.
29 F. Chen, D. Zhang, Q. Yang, X. Wang, B. Dai, X. Li, X. Hao, Y. Ding, J. Si and X. Hou, *Langmuir*, 2010, **27**, 359–365.
30 D. Xia and S. R. J. Brueck, *Nano Lett.*, 2008, **8**, 2819–2824.
31 F. Zhang and H. Y. Low, *Langmuir*, 2007, **23**, 7793–7798.
32 L. Tie, Z. Guo and W. Liu, *J. R. Soc., Interface*, 2015, **453**, 142–150.
33 J. Y. Chung, J. P. Youngblood and C. M. Stafford, *Soft Matter*, 2007, **3**, 1163–1169.

 

34 Z.-C. Shao, Y. Zhao, W. Zhang, Y. Cao and X.-Q. Feng, *Soft Matter*, 2016, **12**, 7977–7982.
35 Z. Zhang, T. Zhang, Y. W. Zhang, K.-S. Kim and H. Gao, *Langmuir*, 2012, **28**, 2753–2760.
36 E. Bittoun and A. Marmur, *Langmuir*, 2012, **28**, 13933–13942.
37 Y. Li, S. Dai, J. John and K. R. Carter, *ACS Appl. Mater. Interfaces*, 2013, **5**, 11066–11073.
38 X. Chen and J. W. Hutchinson, *J. Appl. Mech.*, 2004, **71**, 597–603.
39 E. A. Wilder, S. Guo, S. Lin-Gibson, M. J. Fasolka and C. M. Stafford, *Macromolecules*, 2006, **39**, 4138–4143.
40 H. Jiang, D.-Y. Khang, J. Song, Y. Sun, Y. Huang and J. A. Rogers, *Proc. Natl. Acad. Sci. U. S. A.*, 2007, **104**, 15607–15612.
41 A. Chiche, C. M. Stafford and J. T. Cabral, *Soft Matter*, 2008, **4**, 2360–2364.
42 Y. Zhao, Q. Lu, M. Li and X. Li, *Langmuir*, 2007, **23**, 6212–6217.
43 S. G. Lee, H. S. Lim, D. Y. Lee, D. Kwak and K. Cho, *Adv. Funct. Mater.*, 2013, **23**, 547–553.
44 A. Marmur, *Langmuir*, 2003, **19**, 8343–8348.
45 R. Fürstner, W. Barthlott, C. Neinhuis and P. Walzel, *Langmuir*, 2005, **21**, 956–961.
46 R. Wenzel, *Ind. Eng. Chem. Res.*, 1936, **28**, 988–994.
47 A. B. D. Cassie, *Discuss. Faraday Soc.*, 1948, **3**, 11–16.
48 R. H. Dettre and R. E. Johnson, *Contact Angle, Wettability, and Adhesion*, American Chemical Society, 1964, ch. 8, vol. 43, pp. 136–144.
49 H. Hillborg and U. W. Gedde, *IEEE Trans. Dielectr. Electr. Insul.*, 1999, **6**, 703–717.
50 W. Hong, X. Zhao and Z. Suo, *Appl. Phys. Lett.*, 2009, **95**, 111901.
51 Y. Cao and J. W. Hutchinson, *Proc. R. Soc. A*, 2011, **468**, 94.
52 M. Ben Amar and P. Ciarletta, *J. Mech. Phys. Solids*, 2010, **58**, 935–954.
53 L. Pocivavsek, R. Dellsy, A. Kern, S. Johnson, B. Lin, K. Y. C. Lee and E. Cerda, *Science*, 2008, **320**, 912.
54 J. B. Kim, P. Kim, N. C. Pegard, S. J. Oh, C. R. Kagan, J. W. Fleischer, H. A. Stone and Y.-L. Loo, *Nat. Photonics*, 2012, **6**, 327–332.
55 F. Brau, P. Damman, H. Diamant and T. A. Witten, *Soft Matter*, 2013, **9**, 8177–8186.
56 Y. Ebata, A. B. Croll and A. J. Crosby, *Soft Matter*, 2012, **8**, 9086–9091.
57 J. Zang, X. Zhao, Y. Cao and J. W. Hutchinson, *J. Mech. Phys. Solids*, 2012, **60**, 1265–1279.
58 F. Brau, H. Vandeparre, A. Sabbah, C. Poulard, A. Boudaoud and P. Damman, *Nat. Phys.*, 2011, **7**, 56–60.
59 T. Verho, J. T. Korhonen, L. Sainiemi, V. Jokinen, C. Bower, K. Franze, S. Franssila, P. Andrew, O. Ikkala and R. H. A. Ras, *Proc. Natl. Acad. Sci. U. S. A.*, 2012, **109**, 10210–10213.
60 J. Long, M. N. Hyder, R. Y. M. Huang and P. Chen, *Adv. Colloid Interface Sci.*, 2005, **118**, 173–190.
61 K. Koch, M. Bennemann, H. F. Bohn, D. C. Albach and W. Barthlott, *Bioinspiration Biomimetics*, 2013, **8**, 036005.
62 K. J. Kubiak and T. G. Mathia, *Procedia Eng.*, 2014, **79**, 45–48.
63 Y. Rahmawan, M.-W. Moon, K.-S. Kim, K.-R. Lee and K.-Y. Suh, *Langmuir*, 2009, **26**, 484–491.